Subthreshold repertoire and threshold dynamics of midbrain dopamine neuron firing *in vivo*

Kanako Otomo*[1] & Jessica Perkins*[2],

Anand Kulkarni[2] & Strahinja Stojanovic[1**],**

Jochen Roeper[1#] & Carlos A. Paladini[2#]

1 Institute of Neurophysiology, Neuroscience Center, Goethe University Frankfurt, Germany

2 University of Texas at San Antonio Neurosciences Institute, San Antonio, USA

* shared first authors

** shared second authors

shared senior & communicating authors

Carlos Paladini
University of Texas at San Antonio Neurosciences Institute,
Department of Biology
University of Texas at San Antonio, San Antonio
TX, 78249, USA
carlos.paladini@utsa.edu

Jochen Roeper
Institute of Neurophysiology, Neuroscience Center
Goethe University Frankfurt
Theodor-Stern-Kai 7
60590 Frankfurt, Germany
roeper@em.uni-frankfurt.de

Abstract

The firing pattern of ventral midbrain dopamine neurons is controlled by afferent and intrinsic activity to generate prediction error signals that are essential for reward-based learning. Given the absence of intracellular *in vivo* recordings in the last three decades, the subthreshold membrane potential events that cause changes in dopamine neuron firing patterns remain unknown. By establishing stable *in vivo* whole-cell recordings of >100 spontaneously active midbrain dopamine neurons in anaesthetized mice, we identified the repertoire of subthreshold membrane potential signatures associated with distinct *in vivo* firing patterns. We demonstrate that *in vivo* activity of dopamine neurons deviates from a single spike pacemaker pattern by eliciting transient increases in firing rate generated by at least two diametrically opposing biophysical mechanisms: a transient depolarization resulting in high frequency plateau bursts associated with a reactive depolarizing shift in action potential threshold, and a prolonged hyperpolarization preceding slower rebound bursts characterized by a predictive hyperpolarizing shift in action potential threshold. Our findings therefore illustrate a framework for the biophysical implementation of prediction error coding in dopamine neurons by tuning action potential threshold dynamics.

Main

The midbrain dopamine system is necessary for essential brain functions related to reward-based learning, motivation, action, and cognition (Athalye et al., 2020; Gershman and Uchida, 2019; Langdon et al., 2018; Schultz, 2015). Loss or dysregulation of dopamine neuron subpopulations located in the substantia nigra pars compacta (SNc) and ventral tegmental area (VTA) perturbs crucial circuits leading to major brain disorders, including Parkinson's disease (Obeso et al., 2017), schizophrenia (McCutcheon et al., 2019), depression (Grace, 2016), and addiction (Volkow et al., 2017). However, describing the dynamics of subthreshold ionic conductances that cause dopamine neuron spiking activity *in vivo* has remained a challenge for neurophysiologists.

Single-unit extracellular recording studies from non-human primates and rodents have provided major insights into the computational roles of dopamine neuron firing, most prominently in the context of reward-based learning (Hikosaka et al., 2018; Schultz, 2015, 2016). Dopamine neurons signal prediction errors by transient, sub-second changes in their firing rates. A recent study implied that prediction error coding in dopamine neurons might occur in a distributed manner, thereby creating a range from "optimistic" to "pessimistic" cellular coding schemes (Dabney et al., 2020). For many years, transient cue- or reward-associated increases in firing rate – from a low tonic background frequency (about 1-8 Hz) into the beta and gamma range (15-30 Hz and 40-100 Hz, respectively) – were thought to encode positive reward prediction errors (RPEs), while transient reductions or pauses in baseline firing were believed to encode negative RPEs, induced for instance by the omission of an expected reward. However, increasing experimental evidence points to a multitude of other dopamine functions such as salience

and novelty, action control (Coddington and Dudman, 2018; Jin and Costa, 2010) as well as aversion (Menegas et al., 2018) which are in line with the emerging molecular (Heymann et al., 2020; Poulin et al., 2020), cellular, and anatomical diversity of the midbrain dopamine system (Beier et al., 2019; Beier et al., 2015; Farassat et al., 2019; Lammel et al., 2008; Lammel et al., 2012; Morales and Margolis, 2017; Watabe-Uchida et al., 2012). Even within canonical RPE signaling, the interpretation of the transient burst has become more complex. It is currently divided into a short-latency component, which signals sensory characteristics of the stimulus (e.g. intensity), and a long-latency component, which represents predictive properties of the stimulus (Schultz, 2016). In addition, recent progress has been made in characterizing the underlying arithmetic of single dopamine neurons in the context of RPE signaling (Eshel et al., 2015). It is reasonable to assume that dopamine neurons *in vivo* integrate various heterogeneous afferents throughout the brain (Tian et al., 2016) to tune intrinsic pacemaker activity and generate burst-pause firing patterns, which in turn lead to temporally resolved, extracellular dopamine concentration transients in target regions (Beeler and Kisbye Dreyer, 2019). In addition, mechanisms of dopamine firing synchronization, as well as presynaptic control, are likely to shape axonal dopamine release (Condon et al., 2019). Therefore, dopamine neurons are not simply leaky integrators of excitatory and inhibitory synaptic inputs. They display a rich and diverse repertoire of intrinsic excitability, including biophysical mechanisms for autonomic pacemaker firing.

However, how inputs are integrated *in vivo* at the cellular level has mostly remained unknown for many decades, due to the lack of available tools. While the *in vivo* extracellular recording method does record spontaneous firing patterns generated by

dopamine neurons, it is blind to the causal subthreshold processes that lead to the apparent timed spiking patterns. Intracellular recordings are unique in their ability to directly monitor and manipulate membrane potentials with full temporal resolution. Yet, the only available intracellular *in vivo* data on dopamine neurons came from the pioneering studies by Grace & Bunney in the early eighties (Grace and Bunney, 1980, 1983a, b, 1984a, b). Here, we provide the first data set in nearly four decades on the subthreshold membrane potential behavior *in vivo* associated with firing patterns such as pacemaking and bursting. We established a robust method for deep *in vivo* patch-clamp recordings of dopamine neurons in anaesthetized, adult C57BL/6 mice. Our data set comprises 112 spontaneously active, neurobiotin-labelled and immunocytochemically-identified dopamine neurons, which were mapped to their respective anatomical positions within the SNc and VTA. Unexpected by decades of *in vivo* extracellular recordings, we identified two distinct biophysical subthreshold signatures that drive transient burst firing. We demonstrate that pacemaking dopamine neurons *in vivo* have the ability to tightly control their excitability, as monitored by their action potential thresholds and interspike membrane potentials, and that opposing mechanisms underlying burst discharge are characterized by predictive and reactive shifts in action potential thresholds, and baseline membrane potentials. Thus, our study provides a framework for mechanistic studies into prediction error coding of dopamine neurons in awake and behaving animals.

Results

We obtained *in vivo* whole-cell recordings from 112 spontaneously firing, identified midbrain dopamine neurons in isoflurane-anaesthetized, adult C57BL/6 mice (Fig. 1AB). All neurons included in this study were filled with neurobiotin or biocytin and successfully recovered for anatomical mapping and post-hoc identification as dopaminergic using tyrosine hydroxylase (TH) immunohistochemistry (Fig. 1C). While we densely covered DA neurons in the rostral parabrachial VTA and rostro-medial SNc, we have less DA neurons in lateral aspects of the SNc and in more caudal ventro-medial, paranigral VTA regions (Fig. 1D). TH-immunonegative cells were also encountered, but they were either electrically silent, with membrane potentials below -50 mV, or fast firing (>10 Hz) with narrow action potentials (data not shown), indicating they were unlikely to be dopaminergic. In contrast to extracellular recordings, *in vivo* patch-clamping has no bias toward electrically active cells. Of 116 total recordings, 112 were spontaneously active while 2 were electrically silent, but did fire in response to depolarizing current injection. The remaining 2 dopamine neurons fired less than 1 spontaneous spike per minute (not shown). Figure 1B shows a typical in vivo patch-clamp recording of an identified midbrain dopamine neuron. The recording presented on an expanded time scale displayed episodes of overshooting spikes interspersed by pauses where the membrane potential hyperpolarizes below the threshold for action potentials (Fig. 1B bottom trace). Under isoflurane anesthesia, the technical and biological stabilities of recordings in the whole-cell configuration were not a major limiting factor (Supplemental Figure 1). Also, membrane potential responses to hyperpolarizing current injections were preserved *in vivo* and displayed a diversity reminiscent of previous *in vitro* studies (Supplemental

Figure 2). Indeed, the whole-cell configuration was deliberately converted into outside-out recordings by gentle withdrawal of the patch-pipette. This left an intact biotin-filled dopamine neuron behind, which was successfully recovered for post-hoc neuroanatomical and neurochemical identification. For our example recording in Figure 1B, the corresponding dopamine neuron was identified to be localized in the dorso-rostral VTA (red symbol, Fig. 1CD). As we found no significant differences in mean firing rates and precision between DA neurons recorded in two different C57Bl6 substrains (J and N), between male and female mice, and between two different version of the pipette solution with small differences in estimated free calcium concentrations (40 nM versus 80 nM), we pooled the data (see Supplemental Table 1). Figures 1E and 1F show plot the mean firing rates (FR) and variabilities (quantified as coefficient of variation (CV)), respectively, of spontaneous *in vivo* firing from all dopamine neurons included in this study (n = 112, N = 82). In subset of these neurons we determined their input resistance which had a median of about 300 MΩ (295.2 (225.0 to 343.7) MΩ; n = 36, N = 32; Fig. 1G). This was an order of magnitude higher than previously reported using sharp microelectrodes (Grace and Bunney, 1980 1983a). The high input resistance indicates that differences in intrinsic excitability of dopamine neurons are likely to be much less shunted by an *in vivo* high conductance state observed for other types of neurons (Berg et al., 2007; El Boustani et al., 2007). The instantaneous firing rate range for each identified dopamine neuron indicates a wide range of firing frequencies within dopamine neuron recordings (Fig. 1H).

In vivo patch-clamping enabled the systematic investigation of subthreshold signatures underlying tonic and phasic firing patterns in the intact brain. We found that a majority of neurons fired in a single spiking pattern, similar to our previous *in vivo* extracellular studies of identified dopamine neurons (Farassat et al., 2019; Schiemann et al., 2012). A representative recording and the immunohistochemistry of an *in vivo* pacemaking dopamine neuron located in the VTA is shown in Figures 2AB. The trace with a higher temporal resolution (Fig. 2A, bottom trace) demonstrates the stability of the *in vivo* pacemaker firing mode. To capture the subthreshold characteristics of *in vivo* pacemaking, we plotted the distribution of subthreshold membrane potentials for inter-spike interval (ISI) minima (blue dots, Fig. 2A, C), and action potential thresholds (green dots, Fig 2A, D). Both subthreshold minima and maxima (i.e. threshold) exhibited a narrow unimodal distribution, quantified by their respective unimodality indices (Bimodality coefficient V_{min} = 0.36 ± 0.03; V_{thr} = 0.34 ± 0.05; n = 19, N = 18) and the standard deviations (SD) of the Gaussian fits (V_{min} mean = -42.42 ± 5.36 mV, SD = 1.38 ± 0.63 mV; V_{thr} mean = -30.43 ± 3.44 mV, SD = 0.85 ± 0.2 mV; Figure 2C-D). This demonstrates the capacity of *in vivo* dopamine neurons to maintain their stability in firing, similar to what is observed *in vitro*, even when embedded in active circuits. To examine a potential pattern between subthreshold and firing properties, the membrane potentials of ISI minima and action potential thresholds are plotted against their respective ISI durations (Fig. 2E). While there is more variability in the subthreshold membrane minima as compared to the maxima, the respective ISIs of both plots show the high degree of steady spiking in pacemaking dopamine neurons. Next, we utilized threshold-triggered averaging to obtain a visual representation of a stereotypical subthreshold membrane

potential signature of *in vivo* pacemaking (Fig. 2F). The averaged trace (thick trace in bottom of panel) portrays a subthreshold signature of a ~200 ms gradual, ramp-like membrane potential depolarization of about 10 mV until reaching firing threshold. Figure 2G plots the firing frequency distribution of this cell, and figure 2H that of the entire population of DA neurons identified by their subthreshold properties to discharge in *in vivo* pacemaker mode.

To gain more mechanistic insight, we analyzed the phase plots of action potentials during the respective action potential sequences of pacemaker firing. Figure 2I illustrates an example trace of a sequence of three action potentials (black - orange - red) during pacemaker firing. Examination of the phase plots for all spikes occurring during pacemaker firing from one dopamine neuron are depicted in Figure 2J. Note the large degree of overlap throughout the different phases of the action potentials, from threshold to upstroke and overshoot, as well as during repolarization and afterhyperpolarization. Quantitative analysis of all dopamine neurons discharging in this *in vivo* pacemaker mode (n = 19) confirmed the high degree of stability and low variability that extended from the subthreshold domain to the action potential. Indeed, we did not discover significant changes in threshold voltage, maximal depolarization (Max dV/dt), or repolarization (Min dV/dt) speeds across the sequence of three action potentials (ΔV_{thr}: spike 1 vs 2 = -0.03 (-0.09 to 0.15) mV, spike 2 vs 3 = -0.06 (-0.18 to 0.08) mV; Δ max dV/dt: spike 1 vs 2 = -0.04 (-0.25 to 0.31) V/s, spike 2 vs 1 = -0.0 (-0.29 to 0.19) V/s; p = 0.78, 0.45, 0.38, and 0.58 for all comparisons; n = 19, N = 18; Fig. 2K, Supplemental Table 2).

We then focused our analysis on transient high frequency firing episodes in dopamine SNc/VTA neurons, usually termed “bursts” in dopamine neurons. In contrast to cue- and

reward-triggered bursts in awake animals, *in vivo* burst firing in anesthetized animals has no clear behavioral correlate, and thus seem to occur spontaneously. Moreover, bursts do not only manifest as single events, but often occur in patterns, with some dopamine neurons being locked in a repetitive burst firing mode (Paladini and Tepper, 1999; Schiemann et al., 2012). We focused our analysis on these burst-mode dopamine neurons, which enabled for the first time the unbiased identification and classification of burst-related subthreshold membrane potential signatures without the need for heuristics based on ISI statistics (Bingmer et al., 2011; Grace and Bunney, 1984a; Ko et al., 2012). We were surprised to discover that spontaneous *in vivo* bursting of identified dopamine neurons occurred in association with two diametrically opposed subthreshold membrane potential signatures (compare Figures 3 and 4). The first burst mode was characterized by long and deep hyperpolarizations of the membrane potential, which preceded the transient high frequency discharge (Fig. 3). Accordingly, we termed this mode *rebound burst* firing. When we plotted the distributions of ISI voltage minima (i.e. the most hyperpolarized membrane potential between two action potentials), we noticed that they – in contrast to those of pacemaking dopamine cells – were best described by bimodal gaussian distributions (Fig. 3C). This was quantified by calculating the bimodality coefficient of the ISI voltage minima (V_{min}) distributions for all dopamine neurons with this type of rebound bursting (V_{min} bimodality index = 0.66 ± 0.11; Mode 1 V_{min} mean = -46.03 ± 4.04 mV, SD = 2.76 ± 1.31 mV; Mode 2 V_{min} mean = -39.34 ± 4.45 mV, SD = 1.38 ± 0.36; n = 16, N = 16). Importantly, the V_{min} from the distribution with more hyperpolarized membrane potentials (Mode 1 in Fig. 3C) were almost exclusively associated with longer ISI durations in the range of 640-1120 ms (dark blue circles, Fig. 3E) compared to those

from the more depolarized V_{min} distribution (light blue circles, Fig. 3E). Consequently, these long duration ISI formed an independent cluster of events. In contrast, the distribution of voltage maxima (i.e. action potential thresholds, V_{thr}) in rebound burst dopamine neurons remained unimodal (Fig. 3DE) and much less variable at different ISI durations (V_{thr} mean = -30.07 ± 2.9 mV, SD = 1.44 ± 0.52 mV). Using threshold-triggered averaging of the first spike after Mode 1 V_{min} events (Fig. 3F), a stereotypical (i.e. low variability) subthreshold membrane potential signature of *in vivo* rebound bursting emerges (Fig. 3F lower trace). In contrast, event-triggered averaging of spikes following the Mode 2 V_{min} events did not result in a stereotypical low variability subthreshold waveform (not shown). The rebound subthreshold signature was characterized by a long (546.7 ± 218.4 ms, n = 16, N = 16) symmetrically curved trajectory of initial membrane hyperpolarization (8.2 ± 3.1 mV hyperpolarization to a minimum of -47.8 ± 4.2 mV, n = 16, N = 16) followed by membrane depolarization back to threshold. This rebound burst mode was associated with bursting in the beta frequency range, but also allowed lower frequencies. Thus, the frequency distribution associated with the rebound burst significantly widened the dynamic range of dopamine neurons compared to pacemaking (Median pacemaker firing rate: 6.29 ± 3.96 Hz, $p = 2.43 \times 10^{-262}$ versus rebound burst firing rate; Fig 3G-H). Note that not the rebound-associated frequency distribution of a single dopamine neuron alone (Fig. 3G) but the population of dopamine neurons together cover a larger dynamic range (Fig. 3H). This is in line with the recent idea of a distributed population code for dopamine neurons (Dabney et al., 2020).

In contrast to pacemaking, the phase plots of the rebound burst action potentials show significant differences. In particular, the first action potential of the rebound burst (yellow;

Fig. 3I) has a significantly more hyperpolarized threshold associated concurrently with an accelerated speed of depolarization (Max dV/dt; Fig. 3JK). These changes are consistent with an enhanced excitability, e.g. by increasing the number of available voltage-gated sodium channels set by the membrane hyperpolarization that precedes the onset of the rebound burst. Once within the rebound burst, the threshold returns close to pre-burst baseline already with the next spike as well as the depolarization speed (ΔV_{thr}: spike 1 vs 2 = -2.06 (-3.12 to -1.16) mV, spike 2 vs 3 = 0.85 (0.63 to 1.03) mV; Δ max dV/dt: spike 1 vs 2 = 7.29 (3.42 to 14.51) V/s, spike 2 vs 3 = -2.9 (-4.12 to -1.74) V/s; $p = 1.15 \times 10^{-7}$, 7.05×10^{-7}, $p = 1.15 \times 10^{-7}$, 7.05×10^{-7} for all comparisons; n = 16, N = 16; Fig. 3K, Supplemental Table 2). Thus, the observed threshold dynamics of rebound bursts in dopamine neurons occur at burst onset.

In addition to the rebound burst, we detected qualitatively different subthreshold properties that were exclusively associated with higher frequency bursting. Short bursts in the gamma range were associated with a significant depolarization plateau in membrane potential. Thus, we called this discharge pattern *plateau bursts*. Figure 4AB depicts a typical example of an identified VTA dopamine neuron locked in firing of plateau bursts. The extended time scale shows that in contrast to bursting in rebound mode, the action potential threshold for the plateau burst showed a depolarizing shift of up to 10 mV before burst termination (Fig. 4A, lower panel). While the distributions of ISI minima for plateau busts are complex and were only approximated with bimodal distributions (Fig. 4C; V_{min} Mode1 mean = -39.35 ± 5.23, SD = 2.98 ± 0.7; Mode 2 mean = -27.28 ± 7.16, SD = 1.23 ± 0.38, n = 5, N = 5), the distributions of the threshold voltage are clearly bimodal (Fig. 4D; V_{thr} Mode1 mean = -30.09 ± 5.1, SD = 1.16 ± 0.43; Mode 2 mean = -

22.93 ± 9.08, SD = 2.1 ± 1.02; n = 5, N = 5), a unique feature compared to pacemaking and rebound bursting. Figure 4CD displays the bimodal distribution of these ISI voltage maxima (V_{thr} bimodality index: 0.66 ± 0.16, V_{min} bimodality index: 0.53 ± 0.2; n = 5 cells, N = 5). Those V_{thr} from the 2nd more depolarized distribution (Mode 2 in Fig. 4D) were almost exclusively associated with short intraburst ISI durations in the range of 6-26 ms (light green circles in Fig. 4E). Again, using event-triggered averaging of action potentials associated with Mode 2 in the V_{thr} distributions (Fig. 4F) revealed a distinct and low variability subthreshold signature (Fig. 4F lower trace). What emerges is a sharp-rising and short plateau of about 7 mV in amplitude and 30 ms in duration with a limited number of 2-3 high-frequency gamma-range spikes riding on top (plateau amplitude = 6.31 (4.83 to 9.18) mV; plateau duration = 22.32 (15.4 to 49.77) ms; number of spikes = 2 (2 to 2.18); mean maximum spike frequency = 67.43 (38.4 to 101.69) Hz). Figure 4G plots the firing frequency distribution of the example cell. Figure 4H plots the entire population of dopamine neurons identified by the subthreshold properties to discharge in the plateau burst mode. In contrast to rebound bursts, which enabled both beta range and slower discharge, the plateau burst was restricted to high frequency discharge. In essence, our unbiased exploration of the parameter space at subthreshold membrane voltages of dopamine neurons *in vivo* resulted in the identification of unique subthreshold signatures. These signatures in turn were associated with different dynamic ranges of firing.

In contrast to the rebound burst, we found no change in the threshold potential and action potential waveform properties at the onset of the plateau burst (Fig. 4I-K). This implies that no systematic and in turn predictive threshold dynamics precede the occurrence of plateau bursts in dopamine neurons. Or stated from the neuron's

perspective, they were “surprised” by the burst. However, after plateau burst onset the threshold and action potential dynamics dramatically change, as the 2nd action potential in the burst displays a large depolarizing shift in the threshold potential associated with reduced depolarization speed, both indicators of reduced excitability (Fig. 4JK; ΔV_{thr}: spike 1 vs 2 = 0.61 (-0.04 to 1.0) mV, p = 0.13; spike 2 vs 3 = 6.43 (4.53 to 9.14), p = 0.008; Δ max dV/dt: spike 1 vs 2 = -1.91 (-3.5 to 0.17) V/s, p = 0.13; spike 2 vs 3: -17.24 (-18.13 to -13.81) V/s, p = 0.008; n = 5, N = 5; Supplemental Table 2). Thus, in contrast to the burst in rebound mode, the threshold dynamics of the plateau burst not only occur in the opposite direction but also serve to time the end, not the beginning, of the burst. Indeed, in over 90% percent of all plateau bursts, the 2nd action potential with the large depolarizing shift in threshold was also the last action potential of the burst (plateau bursts with 2 spikes, n = 372; 3 spikes, n = 33; 4 spikes, n = 3). In the remaining cases, only a small amplitude spikelet was observed after the 2nd action potential of the rebound bursts (not shown). Finally, DA neurons locked in plateau bursts were rare and sofar only found in the VTA (Figure 4B), however a much larger percentage of DA neurons generated individual events in the gamma range (Figure 1H). This might imply that DA neurons utilize both burst modes in an alternative fashion.

In summary, the first systematic *in vivo* patch study of identified dopamine SNc/VTA neurons revealed direct evidence of two qualitatively distinct burst mechanisms characterized by stereotypical subthreshold membrane signatures and opposing threshold dynamics. These findings might provide the first framework for how predictive coding is biophysically implemented in midbrain dopamine neurons.

Discussion

For the first time in nearly four decades, we provide new intracellular *in vivo* recordings of identified midbrain dopamine neurons. By establishing deep *in vivo* whole-cell patch-clamp recordings without obvious perturbations on firing activity, our data set allowed the first systematic analysis of the subthreshold membrane potential range of dopamine neurons in the intact brain. We demonstrate that *in vivo* pacemaker-like activity is associated with narrow unimodal distributions of the interspike subthreshold voltage minima and maxima, the latter representing the action potential threshold. In contrast, transient accelerations in firing rate (i.e. bursts) were associated with two distinct subthreshold signatures and threshold dynamics: a faster and shorter depolarization leading to plateau bursts, which were associated with a depolarizing shift in the action potential threshold at the end of the burst; and a preceding membrane hyperpolarization leading up to rebound bursts associated with a hyperpolarizing shift in action potential threshold at the start of the burst. While the plateau burst was strongly coupled to short gamma discharge, the rebound burst was not exclusively associated with beta range bursts, but also allowed lower frequencies. The widening of the dynamic range of dopamine neuron firing by the rebound burst might be an attractive candidate mechanism to enable predictive coding for pacemaking neurons *in vivo*. In particular, the hyperpolarizing shift of the action potential threshold induced by the rebound burst enhances the potential excitability of the neuron and thus enhances the available frequency range. At the same time, the dopamine neuron remains flexible to allow integration of incoming synaptic inputs. Also, the rebound burst spike threshold is distinct from that of the pacemaker background rate, which enables the cell to essentially

compute a new prediction for spike timing. Future *in vivo* whole-cell studies in awake animals are needed to explicitly test whether this candidate subthreshold mechanism is indeed operative during ongoing reward prediction error computations. In contrast, the observed threshold dynamics of the short and high frequency plateau bursts are not predictive, but rather reactive, and might thus serve in burst termination. These features render the plateau burst mechanism an attractive candidate for signaling of unexpected and salient sensory cues by generating a well-timed and short-duration "alerting" signal. While the subthreshold signature of the rebound bursts suggests a timed series of initial inhibition followed by excitation during the predictive time window, short plateau bursts might be generated by rapid fluctuations in the excitation/inhibition (E/I)-balance. Indeed, our previous dynamic clamp studies *in vitro* revealed similar threshold and action potential waveform behavior when the E/I balance rapidly shifts toward more excitation or disinhibition (Lobb et al., 2011). In essence, our study highlights the *in vivo* operating principles of discharging dopamine neurons, and provides explicit candidate mechanisms, which now can be tested in the context of prediction error coding in awake animals.

While the intracellular *in vivo* recordings with sharp microelectrodes of identified dopamine neurons from the nineteen eighties did not provide systematic analyses of the subthreshold membrane potential range in relation to firing patterns, those results are mostly in accordance with our findings. However, there is one important exception. Input resistances in our *in vivo* patch-clamp recordings of dopamine neurons are about 10-fold higher than those reported previously, indicating that the *in vivo* "high conductance" state was overestimated and might be in part attributable to impaling dopamine neurons with

sharp microelectrodes (Grace and Bunney, 1980, 1983a). In addition, it was now possible to carefully determine that the *in vivo* whole-cell configuration did not alter firing patterns observed in intact cells – either with on-cell recordings in this study or by comparison to previous extracellular *in vivo* recordings of identified dopamine neurons (Farassat et al., 2019; Schiemann et al., 2012). Moreover, there are no putative dopamine neurons in this study. All included neurons were filled, recovered, and TH-immunopositive. Given these quality control measures and the large data set, we can also begin to address *in vivo* diversity in dopamine neurons. As previously reported, *in vitro* differences in intrinsic subthreshold properties (Beier et al., 2015; Evans et al., 2017; Lammel et al., 2008; Neuhoff et al., 2002; Tarfa et al., 2017), like sag amplitudes or rebound latencies, were also apparent in our *in vivo* data set, although DA neurons in the paranigral aspect of the VTA were underrepresented. These differences might therefore contribute to subpopulation-specific computations, as recently identified by gCaMP imaging *in vivo* during a complex behavioral task (Engelhard et al., 2019). Moreover, behaviorally relevant somatodendritic computations of dopamine neurons relating to, for example, the current debate of coding motivation and learning (Mohebi et al., 2019) do not necessarily have to cross the action potential threshold (Alle and Geiger, 2006; Christie et al., 2011).

In spite of these strengths, our study has the limitation that we recorded under isoflurane anesthesia and could therefore not study subthreshold membrane potential signatures of behavior-correlated dopamine neuron firing pattern in response to sensory cues and reward-related signals. However, the stability of brain states in controlled anesthesia allowed the unbiased identification of reliable subthreshold signatures associated with relevant burst discharge patterns. Another limitation of our study is that

we did not go beyond the identification of subthreshold patterns in explicitly targeting underlying synaptic and intrinsic biophysical mechanisms. For instance, the rebound burst is preceded by a deep hyperpolarization, which could be activated by different types of synaptic input involving distinct receptors ranging from e.g. $GABA_A$, $GABA_B$, D2R or metabotropic glutamate receptors coupled to small conductance, calcium-activated potassium (SK) channels (Brazhnik et al., 2008; Fiorillo and Williams, 1998; Lacey et al., 1988; Lobb et al., 2011; Lobb et al., 2010; Paladini et al., 2001; Paladini and Tepper, 1999). In addition, the rebound kinetics are likely to be controlled by intrinsic subthreshold excitability, which we demonstrated to be also operative *in vivo* in this study. The relevant balance of rebound depolarization accelerating (e.g. HCN channels (Neuhoff et al., 2002)) and delaying (e.g. Kv4 channels (Subramaniam et al., 2014; Tarfa et al., 2017)) intrinsic conductances is different between dopamine neuron subpopulations, and some respond to the termination of a hyperpolarizing current injection with a robust recruitment of T-type channels (Evans et al., 2017; Wolfart and Roeper, 2002). The plateau burst is driven by a rapid onset depolarization, which is likely to be caused by a fast change in the E/I balance (Lobb et al., 2010). Most likely, the rebound and plateau bursts represent responses in dopamine neurons that are comprised of a sequence of integration of the synaptic inputs that are active at any moment in the intact brain, and the intrinsic cellular processes that are particular to the individual neuron. The *in vivo* patch-clamp method in dopamine neurons will facilitate future mechanistic studies in awake animals, as not only the intracellular milieu (e.g. calcium buffering) can be directly controlled, but also pharmacological agents can be directly applied. The opposing biophysical mechanisms

underlying rebound and plateau bursts provide the first framework for how coding might be biophysically implemented in midbrain dopamine neurons.

Materials & Methods

Animals: C57BL/6N (Charles River Laboratories) and C57BL/6J (Jackson Laboratories) mice (male 67 and female 7, aged 8-16 weeks) were used for the experiments. Neither sex nor strain showed significant differences (Supplemental Table 1) so data were pooled. Mice were maintained on a 12-hour light/dark cycle with food and water available ad libitum. All experimental procedures were approved by the German Regional Council of Darmstadt (TVA 54-19c20/15-F40/28) or the University of Texas at San Antonio Institutional Animal Care and Use Committees.

In vivo electrophysiology: Animals were maintained under isoflurane (1.0-1.5% in 100% O2, 0.35L/min) and head-fixed to a customized recording platform (Luigs & Neumann). After induction, isoflurane levels were adapted to result in a target breathing rate of ≈1 Hz. Craniotomies and duratomies were performed at the reference locations. Upon having a recording pipette reach the correct stereotaxic coordinates and depth (≥ 4 mm from the surface of the brain; e.g. Fig. 1D) recordings were performed. Prior to rupturing the cell membrane for a whole-cell recording, impulse activity – if present – was observed in the cell-attached patch mode. Whole-cell patch clamp recordings were performed using glass electrodes (5-10 MΩ) filled with internal solution containing (in mM): 135 K-gluconate, 10 HEPES, 5 KCl, 5 MgCl2, 0.1 EGTA, 0.075 CaCl2 (variant 1) or no added CaCl2 (variant 2), 5 ATP (Na), and 1 GTP (Li), neurobiotin or biocytin, at pH 7.35. The estimated free calcium concentrations based on a calcium contamination of 15

µm (for details see (Woehler et al., 2014)) were about 40 nM for variant 1 and about 80 nM for variant 2.

Recording electrodes were made with borosilicate glass capillaries (G120F-4, Warner Instruments) pulled with a pipette puller (DMZ Universal Electrode Puller, Zeitz-Instruments). Recording signals were obtained with a patch clamp amplifier (EPC10 USB, HEKA; Multiclamp 700B, Molecular Devices) and the data were acquired with PatchMaster software (HEKA) or Axograph software (Axograph) at a sampling rate of 20kHz. A tone generator (PSA-12, HEKA; Custom script, Axograph) was used to monitor the seal resistance. The electrode was lowered down to approximately 200 µm above the region of interest with a positive pressure of approximately 1000 mBar. The pressure was gradually lowered and kept in a range between 40-70 mbar during probing for cells in the VTA (DV: 4.0-5.2 mm) and SNc (DV: 3.8-5.2 mm). The proximity of cells was detected by a 20-50% increase of pipette resistance. After making a giga-ohm seal, both firing rate and action potential half width were measured using on-cell recordings before breaking into the whole-cell configuration. After applying a small suction to break into the whole-cell mode, cell capacitance and series resistance were estimated in voltage-clamp. Cells were then switched to current-clamp mode to record spontaneous activity and responses to hyperpolarizing current injections.

During all whole-cell recordings, neurons were labeled intracellularly with biocytin (3%) or neurobiotin (0.1%), which was included in the recording pipette. At the end of the recording session, mice were sacrificed for transcardial perfusion-fixation with 4% PFA-PBS, as previously described (Farassat et al., 2019). Brains were removed, post-fixed in 4% PFA-PBS overnight and stored at 4 degrees for later sectioning. Slices were

processed for visualization of tyrosine hydroxylase (TH) and biocytin/neurobiotin for definitive identification of the recorded neurons as TH-positive and for mapping of their locations within VTA and SNc.

Spike detection and spike threshold algorithm: Spike peaks were detected first. Overall, a spike at its threshold was detected when a high dV/dt value was followed by a high voltage value and a low dV/dt value. Specifically, a spike peak was detected if these three conditions were met within a 3 ms window following the crossing of a dV/dt threshold (default value = 10mV/ms). Firstly, the minimal value of dv/dt must be less than -5 mV/ms. Secondly, the maximal value of voltage must be within 30 mV of the highest voltage in the whole trace, and lastly, the difference between the maximal voltage and the voltage at dV/dt-threshold crossing (spike height) must be greater than 5mV. All the parameters mentioned here are tunable and were changed to improve spike detection performance in some cells.

Histology and microscopy: After recording, animals were injected with a lethal dose of pentobarbital (0.3-0.4mL) and transcardially-perfused with PBS followed by 4% paraformaldehyde (wt/vol) and 15% picric acid (vol/vol) in phosphate-buffered saline. Collected brains were post-fixed overnight. Immunocytochemistry and confocal microscopy were performed as previously described (Schiemann et al., 2012). For the tyrosine hydroxylase (TH) staining, polyclonal rabbit antibody (catalog no.657012, Merck) was used as the primary antibody, and AlexaFluor-488 goat anti-rabbit IgG (catalog no.11008, ThermoFisher) as the secondary antibody. Neurobiotin and biocytin were

visualized with AlexaFluor-568 streptavidin conjugate (catalog no. S11226, ThermoFisher).

Quantification and statistical analysis: Recorded values for whole-cell recordings were corrected for liquid junction potential (ca. -12mV). Data processing and quantifications were performed using MATLAB (MathWorks). Wilcoxon Rank sums tests were used to determine statistical differences using MATLAB (MathWorks). Graphs and maps were created using MATLAB or Prism 6. Bimodality coefficient was used for dual process detection (Freeman and Dale, 2013). Measurements of effect size were also calculated (Hentschke and Stuttgen, 2011). Parametric data were presented as mean ± standard deviation. Non-parametric data were presented as median with interquartile range.

Data availability

Access to all original patch-clamp data files, immunohistochemical and anatomical data of identified dopamine neurons, as well as Matlab scripts for analysis, will be provided upon full publication.

Acknowledgements

We are grateful to Nao Uchida, who helped to define the relevant *in vivo* patch-clamp recording parameters of dopamine neurons. We thank Kaue M. Costa for help with confocal imaging and initial mapping of DA neurons. We are grateful for excellent technical support by Jasmine Sontag and Bea Fischer (Neurophysiology, Goethe University). We thank Dr. Gerard Beaudoin for custom scripting of Axograph tone

generation. This work was funded by grants to JR (DFG CRC1080, CRC1193 & NIH DA041705) and CP (NIH MH113341, MH107229).

Author Information

JR & CP designed the study and established the technique for stable in vivo patch-clamp recordings of identified dopamine neurons during a sabbatical of CP in Frankfurt. KO, JP and CP recorded and labeled dopamine neurons in this study. Analysis was carried out by AK, SS, JP & KO supervised by JR & CP.

Ethics Declaration

Authors declare no conflict of interests

Figure Legends

Figure 1. *In vivo* whole cell recordings of identified ventral mesencephalon dopamine neurons. **A.** Schematic representation of the experimental setup. **B.** Representative recording of spontaneous *in vivo* electrical activity from a whole-cell-recorded and neurochemically-identified dopamine neuron in the ventral tegmental area (VTA) of an adult C57Bl/6J mouse under isoflurane anesthesia. The upper trace displays action potentials with overshoot during a stable recording for > 5 minutes. The higher temporal resolution of the electrical activity in the lower trace allows visual identification of subthreshold events such as large hyperpolarizations and synaptic events. **C.** Immunocytochemical identification demonstrates the recorded neuron (top panel, filled with Biocytin; red) is positive for tyrosine hydroxylase (TH; green). Lower magnification of the immunocytochemical image (lower panel) locates the recorded neuron (arrow) within the dorsal region of the VTA. **D**. Depiction shows the location of the recorded neuron (large red dot) in relation to all the recorded neurons in this study (gray dots) displayed at three coronal planes. Bottom right panel is a 3D representation of the example cell location (red sphere) in relation to all recorded cells (gray spheres). **E, F.** Plot of the mean firing rate (E) and coefficient of variation (CV) for interspike intervals (F) for each neuron presented in this study (horizontal line = median). **G.** Plot of the input resistance for each neuron where resistance was measured (horizontal line = median). **H.** Log-scale plot of the instantaneous firing rate, and its full range, for each neuron presented in this study sorted in the order of increasing median rate. **D-H.** The large red symbol in all plots represents the example neuron illustrated in B and C.

Figure 2. Pacemaker pattern is characterized by a stable and narrow subthreshold membrane potential dynamic range. **A**. Representative recording of spontaneous *in vivo* electrical activity from a whole-cell-recorded and neurochemically-identified midbrain dopamine neuron in the VTA. The upper trace displays action potentials with overshoot during a stable recording for > 60 s. The higher temporal resolution of the electrical activity in the lower trace allows visual identification of subthreshold events. Blue dots represent the most hyperpolarized membrane potential (Minima) reached in between every action potential. Green dots represent the most depolarized membrane potential (Maxima; action potential threshold) reached in between every action potential. **B.** Immunocytochemical identification demonstrates the recorded neuron (red) as TH-positive (green). Lower magnification of the image locates the recorded neuron (arrow) within the dorsal region of the VTA. The depiction shows the location of the recorded neuron (large red dot) in relation to all the recorded neurons in this study (gray and black dots). Black dots represent the locations of all the neurons that fired in a pacemaker pattern. **C.** Distribution of all subthreshold voltage minima (V_{min}) from the cell in A-B, demonstrating a unimodal distribution (blue line = single Gaussian fit). **D.** Distribution of all subthreshold voltage maxima (V_{thr}) from the cell in A-B, demonstrating a unimodal distribution (green line = single Gaussian fit). **E.** Scatter plot of the interspike interval (ISI) versus V_{min} (blue) and V_{thr} (green). Longer duration ISIs are correlated with more hyperpolarized voltage minima. **F.** High temporal resolution of pacemaker firing pattern (upper panel), and a mean spike-triggered pacemaker pattern (black trace in lower panel) with overlaid (gray) traces. **G.** Probability histogram of the instantaneous firing rate for the

cell in A-B. **H.** Probability histogram of instantaneous firing rate for all cells firing in a pacemaker pattern. **I.** Example trace of a cell firing in a pacemaker pattern with three action potentials in order from black, then yellow, then red. Inset illustrates where the threshold occurs for the black action potential. **J.** The phase plots for each action potential are displayed in the same color scheme as in I (black, yellow, red; plots are nearly completely overlapping). **K.** Summary data of the changes in threshold voltage (left) and maximal depolarization rate (Max dV/dt; right) across the sequence of three action potentials for all cells firing in a pacemaker pattern.

Figure 3. Rebound burst is characterized by a large hyperpolarization and a hyperpolarizing action potential threshold. **A**. Representative recording of an identified dopamine neuron in the SNc. The upper trace displays action potentials with overshoot during a stable recording for > 60 s. The higher temporal resolution in the lower trace allows visual identification of subthreshold events. Blue dots represent the Minima reached in between every action potential. The dark blue dots represent the minima of large hyperpolarizations. Green dots represent the Maxima (i.e. action potential threshold). **B.** Immunocytochemical identification (top panel) demonstrates the recorded neuron (red) as TH-positive (green). Lower magnification image (middle panel) locates the neuron (arrow) within the SNc. The depiction (bottom panel) shows the location of the recorded neuron (large red dot) in relation to all the recorded neurons (gray and black dots). Black dots represent the locations of all neurons that fired in a rebound burst pattern. **C.** Distribution of subthreshold voltage minima (V_{min}) from the cell in A-B, demonstrating a bimodal distribution (dark blue line = Mode 1 Gaussian fit; light blue line

= Mode 2 Gaussian fit). **D.** Distribution of subthreshold voltage maxima (V_{thr}) from the cell in A-B, demonstrating a unimodal distribution (green line = single Gaussian fit). **E.** Scatter Plot of ISI versus V_{min} and V_{thr}. The dark blue cluster is associated with more hyperpolarized voltage membrane potentials and longer duration ISIs. **F.** High temporal resolution of a rebound burst (upper panel), and event-triggered rebound burst average (lower panel, black trace) and overlaid (gray) traces. **G.** Probability histogram of the cell firing rate associated with rebound bursts. **H.** Probability histogram of firing associated with rebound bursts for all cells that fired in a rebound burst pattern. **I.** Example trace of a cell firing a rebound burst with three action potentials in order from black prior to the burst, then yellow beginning the burst, and red. Inset illustrates where the hyperpolarized threshold (K) occurs for the action potential beginning the burst (yellow). **J.** The phase plots for each action potential are displayed in the same color scheme as in I. **K.** Summary data of the changes in threshold voltage (left) with significant hyperpolarization in threshold of the first action potential of the burst (yellow), and change in maximal depolarization rate (Max dV/dt; middle) with significant increase in Max dV/dt, across the sequence of three action potentials for all cells firing in a rebound burst pattern.

Figure 4. Plateau burst is characterized by a plateau depolarization and a depolarizing action potential threshold. **A**. Representative recording of a dopamine neuron in the VTA. The upper trace displays action potentials with overshoot during a stable recording for > 60 s. The higher temporal resolution in the lower trace allows visual identification of subthreshold events. Dark blue dots represent more hyperpolarized voltage minima whereas light blue dots represent minima occurring during plateaus. Dark green dots

represent the subthreshold voltage maxima with the more depolarized threshold depicted by light green dots. **B.** Immunocytochemical identification (upper panel) demonstrates the recorded neuron (red) is TH-positive (green). Lower magnification image (middle panel) locates the recorded neuron (arrow) within the VTA. Depiction (bottom panel) shows the location of the recorded neuron (large red dot) in relation to all the recorded neurons in this study (gray and black dots). Black dots represent neurons that fired in a plateau burst pattern. **C.** Distribution of all subthreshold voltage minima (V_{min}) from the cell in A-B, demonstrating a bimodal distribution (dark blue line = Mode 1 Gaussian fit; light blue line = Mode 2 Gaussian fit). **D.** Distribution of all subthreshold voltage maxima (V_{thr}) from the cell in A-B, demonstrating a bimodal distribution (black line = Mode 1 Gaussian fit; yellow line = Mode 2 Gaussian fit). **E.** Scatter plot of ISI versus V_{min} and V_{thr}. The light green cluster is associated with more depolarized voltage membrane potentials and shorter duration ISIs. **F.** High temporal resolution of a plateau burst (upper panel), and event-triggered plateau burst average (black trace in lower panel) and overlaid (gray) traces. **G.** Probability histogram of the firing rate associated with plateau bursts for the example cell in A-B. **H.** Probability histogram of firing rate associated with plateau bursts for all cells. **I.** Example trace of a cell firing a plateau burst with three action potentials in order from black prior to the burst, then yellow beginning the burst, and finally red ending the burst. Inset illustrates where the depolarized threshold (K) occurs for the action potential ending the burst (red). **J.** The phase plots for each action potential are displayed in the same color scheme as in I. **K.** Summary data of the changes in threshold voltage (left) with significant depolarization in threshold of the action potential ending the burst (red),

change in maximal depolarization rate (Max dV/dt; middle) with significant decrease in Max dV/dt of the last action potential (red) for all cells firing in a plateau burst pattern.

Supplemental Figure 1. *In vivo* whole-cell recording of dopamine neurons does not disturb firing rate or pattern of activity. **A.** Representative recording of spontaneous *in vivo* electrical activity from a neuron recorded in on-cell mode (upper trace) and then broken into the whole-cell configuration (lower trace) with similar firing rate and pattern. **B.** Immunocytochemical identification (top panel) demonstrates the recorded, biocytin-filled neuron (B; red) is positive for tyrosine hydroxylase (TH; green). Lower magnification image (middle panel) locates the recorded neuron (arrow) within the medial region of the SNC. The depiction (lower panel) shows the location of the recorded neuron (large red dot) in relation to all the recorded neurons in this study (black and gray dots). Black dots represent all cells for which on-cell activity was recorded for comparison with whole-cell activity. **C.** Time series of mean firing rate during the transition from on-cell to whole-cell modes (vertical dashed line at time = 0; on-cell mean rate = 4.27 (3.18 to 5.75) Hz; whole-cell mean-rate = 5.76 (3.92 to 6.56) Hz; n = 19, N = 16; p = 0.11). **D.** Time series of mean firing rate for the first 100 seconds from all neurons recorded in this study (slope change in FR = -0.005; n = 110, N = 78). **E.** Time series of the coefficient of variation (CV) of firing during the transition from on-cell to whole-cell mode (vertical dashed line at time = 0; on-cell CV = 0.69 (0.42 to 0.82); whole-cell CV = 0.51 (0.34 to 0.77); n = 19, N =16; p = 0.38). **F.** Time series of firing CV for the first 100 seconds from all neurons recorded in this study (slope change in CV = 0.003; n = 110, N = 78). **C-F.** Red line represents the example neuron illustrated in A and B. Black line represents the average of all lines for each panel.

Supplemental Figure 2. Sag and rebound delay are correlated with cell location. **A.** Example recording from an identified dopamine neuron with a large sag in response to hyperpolarizing current injection, and a short delay to the first spike upon removal of the hyperpolarization (blue arrowhead). **A-C.** The immunocytochemical image shows the location (arrow) of the recorded neuron. **B.** Example recording from an identified dopamine neuron with a moderate sag in response to hyperpolarizing current injection, and a moderate delay to the first spike upon removal of the hyperpolarization (pink arrowhead). **C.** Example recording from an identified dopamine neuron with almost no sag in response to hyperpolarizing current injection, and a long delay to the first spike upon removal of the hyperpolarization (orange arrowhead). **D,F.** Plots of the input resistance (D) and rebound delay (F) for all neurons where the relevant protocols were carried out (sag amplitude at -80 mV = 8.16 ± 4.41 mV; n = 60, N = 50; rebound delay = 84.55 (52.84 to 146.44) ms; n = 60, N = 50). **E,G.** Relationship of cell location with sag amplitude and rebound delay. Both measures had a significant relationship with location in the dorsal-ventral and rostral-caudal planes. **D-G.** Large dots are colored in correspondence with the arrowhead colors in A-C.

Supplemental Data Table 1

Table showing that there are no-significant differences in firing rate and CV of ISI between various groupings of cells:

- Cells from male vs female animals
- Recordings made using internal solution containing 40nM vs 80nM free calcium
- Cell from animals belonging to sub-strains C57BL/6N vs C57BL/6J.

All values are reported as [median (25th quantile-75th quantile)] and all p-values are reported for the Wilcoxon rank sum test. Upper-case letter 'N' indicates the numbers of animals and the lower-case letter 'n' indicates the number of cells in that grouping.

Comparison type	**FR (Hz)**			**CV**		
Male (n=93, N=67) vs Female (n=12, N=7)	**m**	**f**	**p-value**	**m**	**f**	**p-value**
	5.23(3.65-6.72)	6.07(4.38-7.2)	0.31	0.43(0.3-0.67)	0.45(0.41-0.58)	0.45
Ca^{++}40nM (n=8, N=6) vs 80nM (n=104, N=74)	**40**	**80**	**p-value**	**40**	**80**	**p-value**
	3.86 (1.0-6.12)	5.26 (3.59-6.8)	0.15	0.45 (0.39-0.66)	0.42 (0.3-0.65)	0.71
C57BL/6N (n=92, N=65) vs C57BL/6J (n=20, N=15)	**N**	**J**	**p-value**	**N**	**J**	**p-value**
	5.09(3.46-6.8)	5.39(3.61-6.62)	0.94	0.41(0.26-0.62)	0.49(0.39-0.68)	0.15

Supplemental Data Table 2

Table showing trajectories of repolarization speed (min dV/dt) across three types of spiking activity patterns. All values are reported as [median (25th quantile-75th quantile)] and all p-values are reported for the Wilcoxon rank sum test.

Spiking pattern	**min dV/dt spike 1 vs spike 2 (V/s)**		**min dV/dt spike 2 vs spike 3 (V/s)**	
Pacemaker	**Magnitude**	**p-value**	**Magnitude**	**p-value**
	0.03 (-0.09 to 0.21)	0.78	-0.0 (-0.16 to 0.08	0.45
Rebound burst	**Magnitude**	**p-value**	**Magnitude**	**p-value**
	-3.6 (-6.85 to -2.21)	1.15×10^{-7}	2.03 (1.26 to 2.86)	7.05×10^{-7}
Plateau burst	**Magnitude**	**p-value**	**Magnitude**	**p-value**
	0.94 (-0.67 to 1.84)	0.68	7.35 (6.66 to 9.68)	0.008

References

Alle, H., and Geiger, J.R. (2006). Combined analog and action potential coding in hippocampal mossy fibers. Science 311, 1290-1293.

Athalye, V.R., Carmena, J.M., and Costa, R.M. (2020). Neural reinforcement: re-entering and refining neural dynamics leading to desirable outcomes. Curr Opin Neurobiol 60, 145-154.

Beeler, J.A., and Kisbye Dreyer, J. (2019). Synchronicity: The Role of Midbrain Dopamine in Whole-Brain Coordination. eNeuro 6.

Beier, K.T., Gao, X.J., Xie, S., DeLoach, K.E., Malenka, R.C., and Luo, L. (2019). Topological Organization of Ventral Tegmental Area Connectivity Revealed by Viral-Genetic Dissection of Input-Output Relations. Cell Rep 26, 159-167 e156.

Beier, K.T., Steinberg, E.E., DeLoach, K.E., Xie, S., Miyamichi, K., Schwarz, L., Gao, X.J., Kremer, E.J., Malenka, R.C., and Luo, L. (2015). Circuit Architecture of VTA Dopamine Neurons Revealed by Systematic Input-Output Mapping. Cell 162, 622-634.

Berg, R.W., Alaburda, A., and Hounsgaard, J. (2007). Balanced inhibition and excitation drive spike activity in spinal half-centers. Science 315, 390-393.

Bingmer, M., Schiemann, J., Roeper, J., and Schneider, G. (2011). Measuring burstiness and regularity in oscillatory spike trains. J Neurosci Methods 201, 426-437.

Brazhnik, E., Shah, F., and Tepper, J.M. (2008). GABAergic afferents activate both GABAA and GABAB receptors in mouse substantia nigra dopaminergic neurons in vivo. J Neurosci 28, 10386-10398.

Christie, J.M., Chiu, D.N., and Jahr, C.E. (2011). Ca(2+)-dependent enhancement of release by subthreshold somatic depolarization. Nat Neurosci 14, 62-68.

Coddington, L.T., and Dudman, J.T. (2018). The timing of action determines reward prediction signals in identified midbrain dopamine neurons. Nat Neurosci 21, 1563-1573.

Condon, M.D., Platt, N.J., Zhang, Y.F., Roberts, B.M., Clements, M.A., Vietti-Michelina, S., Tseu, M.Y., Brimblecombe, K.R., Threlfell, S., Mann, E.O., and Cragg, S.J. (2019). Plasticity in striatal dopamine release is governed by release-independent depression and the dopamine transporter. Nat Commun 10, 4263.

Dabney, W., Kurth-Nelson, Z., Uchida, N., Starkweather, C.K., Hassabis, D., Munos, R., and Botvinick, M. (2020). A distributional code for value in dopamine-based reinforcement learning. Nature 577, 671-675.

de Jong, J.W., Afjei, S.A., Pollak Dorocic, I., Peck, J.R., Liu, C., Kim, C.K., Tian, L., Deisseroth, K., and Lammel, S. (2019). A Neural Circuit Mechanism for Encoding Aversive Stimuli in the Mesolimbic Dopamine System. Neuron 101, 133-151 e137.

El Boustani, S., Pospischil, M., Rudolph-Lilith, M., and Destexhe, A. (2007). Activated cortical states: experiments, analyses and models. J Physiol Paris 101, 99-109.

Engelhard, B., Finkelstein, J., Cox, J., Fleming, W., Jang, H.J., Ornelas, S., Koay, S.A., Thiberge, S.Y., Daw, N.D., Tank, D.W., and Witten, I.B. (2019). Specialized coding of sensory, motor and cognitive variables in VTA dopamine neurons. Nature 570, 509-513.

Eshel, N., Bukwich, M., Rao, V., Hemmelder, V., Tian, J., and Uchida, N. (2015). Arithmetic and local circuitry underlying dopamine prediction errors. Nature 525, 243-246.

Evans, R.C., Zhu, M., and Khaliq, Z.M. (2017). Dopamine Inhibition Differentially Controls Excitability of Substantia Nigra Dopamine Neuron Subpopulations through T-Type Calcium Channels. J Neurosci 37, 3704-3720.

Farassat, N., Costa, K.M., Stojanovic, S., Albert, S., Kovacheva, L., Shin, J., Egger, R., Somayaji, M., Duvarci, S., Schneider, G., and Roeper, J. (2019). In vivo functional diversity of midbrain dopamine neurons within identified axonal projections. Elife 8.

Fiorillo, C.D., and Williams, J.T. (1998). Glutamate mediates an inhibitory postsynaptic potential in dopamine neurons. Nature 394, 78-82.
Freeman, J.B., and Dale, R. (2013). Assessing bimodality to detect the presence of a dual cognitive process. Behav Res Methods 45, 83-97.
Gershman, S.J., and Uchida, N. (2019). Believing in dopamine. Nat Rev Neurosci 20, 703-714.
Grace, A.A. (2016). Dysregulation of the dopamine system in the pathophysiology of schizophrenia and depression. Nat Rev Neurosci 17, 524-532.
Grace, A.A., and Bunney, B.S. (1980). Nigral dopamine neurons: intracellular recording and identification with L-dopa injection and histofluorescence. Science 210, 654-656.
Grace, A.A., and Bunney, B.S. (1983a). Intracellular and extracellular electrophysiology of nigral dopaminergic neurons--1. Identification and characterization. Neuroscience 10, 301-315.
Grace, A.A., and Bunney, B.S. (1983b). Intracellular and extracellular electrophysiology of nigral dopaminergic neurons--2. Action potential generating mechanisms and morphological correlates. Neuroscience 10, 317-331.
Grace, A.A., and Bunney, B.S. (1984a). The control of firing pattern in nigral dopamine neurons: burst firing. J Neurosci 4, 2877-2890.
Grace, A.A., and Bunney, B.S. (1984b). The control of firing pattern in nigral dopamine neurons: single spike firing. J Neurosci 4, 2866-2876.
Hentschke, H., and Stuttgen, M.C. (2011). Computation of measures of effect size for neuroscience data sets. Eur J Neurosci 34, 1887-1894.
Heymann, G., Jo, Y.S., Reichard, K.L., McFarland, N., Chavkin, C., Palmiter, R.D., Soden, M.E., and Zweifel, L.S. (2020). Synergy of Distinct Dopamine Projection Populations in Behavioral Reinforcement. Neuron 105, 909-920 e905.
Hikosaka, O., Ghazizadeh, A., Griggs, W., and Amita, H. (2018). Parallel basal ganglia circuits for decision making. J Neural Transm (Vienna) 125, 515-529.
Jin, X., and Costa, R.M. (2010). Start/stop signals emerge in nigrostriatal circuits during sequence learning. Nature 466, 457-462.
Knowlton, C., Kutterer, S., Roeper, J., and Canavier, C.C. (2018). Calcium dynamics control K-ATP channel-mediated bursting in substantia nigra dopamine neurons: a combined experimental and modeling study. Journal of neurophysiology 119, 84-95.
Ko, D., Wilson, C.J., Lobb, C.J., and Paladini, C.A. (2012). Detection of bursts and pauses in spike trains. J Neurosci Methods 211, 145-158.
Lacey, M.G., Mercuri, N.B., and North, R.A. (1988). On the potassium conductance increase activated by GABAB and dopamine D2 receptors in rat substantia nigra neurones. J Physiol 401, 437-453.
Lammel, S., Hetzel, A., Hackel, O., Jones, I., Liss, B., and Roeper, J. (2008). Unique properties of mesoprefrontal neurons within a dual mesocorticolimbic dopamine system. Neuron 57, 760-773.
Lammel, S., Lim, B.K., Ran, C., Huang, K.W., Betley, M.J., Tye, K.M., Deisseroth, K., and Malenka, R.C. (2012). Input-specific control of reward and aversion in the ventral tegmental area. Nature 491, 212-217.
Langdon, A.J., Sharpe, M.J., Schoenbaum, G., and Niv, Y. (2018). Model-based predictions for dopamine. Curr Opin Neurobiol 49, 1-7.
Lobb, C.J., Troyer, T.W., Wilson, C.J., and Paladini, C.A. (2011). Disinhibition bursting of dopaminergic neurons. Frontiers in systems neuroscience 5, 25.
Lobb, C.J., Wilson, C.J., and Paladini, C.A. (2010). A dynamic role for GABA receptors on the firing pattern of midbrain dopaminergic neurons. Journal of neurophysiology 104, 403-413.
McCutcheon, R.A., Abi-Dargham, A., and Howes, O.D. (2019). Schizophrenia, Dopamine and the Striatum: From Biology to Symptoms. Trends Neurosci 42, 205-220.

Menegas, W., Akiti, K., Amo, R., Uchida, N., and Watabe-Uchida, M. (2018). Dopamine neurons projecting to the posterior striatum reinforce avoidance of threatening stimuli. Nat Neurosci 21, 1421-1430.
Mohebi, A., Pettibone, J.R., Hamid, A.A., Wong, J.T., Vinson, L.T., Patriarchi, T., Tian, L., Kennedy, R.T., and Berke, J.D. (2019). Dissociable dopamine dynamics for learning and motivation. Nature 570, 65-70.
Morales, M., and Margolis, E.B. (2017). Ventral tegmental area: cellular heterogeneity, connectivity and behaviour. Nat Rev Neurosci 18, 73-85.
Neuhoff, H., Neu, A., Liss, B., and Roeper, J. (2002). I(h) channels contribute to the different functional properties of identified dopaminergic subpopulations in the midbrain. J Neurosci 22, 1290-1302.
Obeso, J.A., Stamelou, M., Goetz, C.G., Poewe, W., Lang, A.E., Weintraub, D., Burn, D., Halliday, G.M., Bezard, E., Przedborski, S*., et al.* (2017). Past, present, and future of Parkinson's disease: A special essay on the 200th Anniversary of the Shaking Palsy. Mov Disord 32, 1264-1310.
Paladini, C.A., Fiorillo, C.D., Morikawa, H., and Williams, J.T. (2001). Amphetamine selectively blocks inhibitory glutamate transmission in dopamine neurons. Nat Neurosci 4, 275-281.
Paladini, C.A., and Tepper, J.M. (1999). GABA(A) and GABA(B) antagonists differentially affect the firing pattern of substantia nigra dopaminergic neurons in vivo. Synapse 32, 165-176.
Poulin, J.F., Gaertner, Z., Moreno-Ramos, O.A., and Awatramani, R. (2020). Classification of Midbrain Dopamine Neurons Using Single-Cell Gene Expression Profiling Approaches. Trends Neurosci 43, 155-169.
Schiemann, J., Schlaudraff, F., Klose, V., Bingmer, M., Seino, S., Magill, P.J., Zaghloul, K.A., Schneider, G., Liss, B., and Roeper, J. (2012). K-ATP channels in dopamine substantia nigra neurons control bursting and novelty-induced exploration. Nat Neurosci 15, 1272-1280.
Schultz, W. (2015). Neuronal Reward and Decision Signals: From Theories to Data. Physiol Rev 95, 853-951.
Schultz, W. (2016). Dopamine reward prediction-error signalling: a two-component response. Nat Rev Neurosci 17, 183-195.
Subramaniam, M., Althof, D., Gispert, S., Schwenk, J., Auburger, G., Kulik, A., Fakler, B., and Roeper, J. (2014). Mutant alpha-synuclein enhances firing frequencies in dopamine substantia nigra neurons by oxidative impairment of A-type potassium channels. J Neurosci 34, 13586-13599.
Tarfa, R.A., Evans, R.C., and Khaliq, Z.M. (2017). Enhanced Sensitivity to Hyperpolarizing Inhibition in Mesoaccumbal Relative to Nigrostriatal Dopamine Neuron Subpopulations. J Neurosci 37, 3311-3330.
Tian, J., Huang, R., Cohen, J.Y., Osakada, F., Kobak, D., Machens, C.K., Callaway, E.M., Uchida, N., and Watabe-Uchida, M. (2016). Distributed and Mixed Information in Monosynaptic Inputs to Dopamine Neurons. Neuron 91, 1374-1389.
Volkow, N.D., Wise, R.A., and Baler, R. (2017). The dopamine motive system: implications for drug and food addiction. Nat Rev Neurosci 18, 741-752.
Watabe-Uchida, M., Zhu, L., Ogawa, S.K., Vamanrao, A., and Uchida, N. (2012). Whole-brain mapping of direct inputs to midbrain dopamine neurons. Neuron 74, 858-873.
Woehler, A., Lin, K.H., and Neher, E. (2014). Calcium-buffering effects of gluconate and nucleotides, as determined by a novel fluorimetric titration method. J Physiol 592, 4863-4875.
Wolfart, J., and Roeper, J. (2002). Selective coupling of T-type calcium channels to SK potassium channels prevents intrinsic bursting in dopaminergic midbrain neurons. J Neurosci 22, 3404-3413.

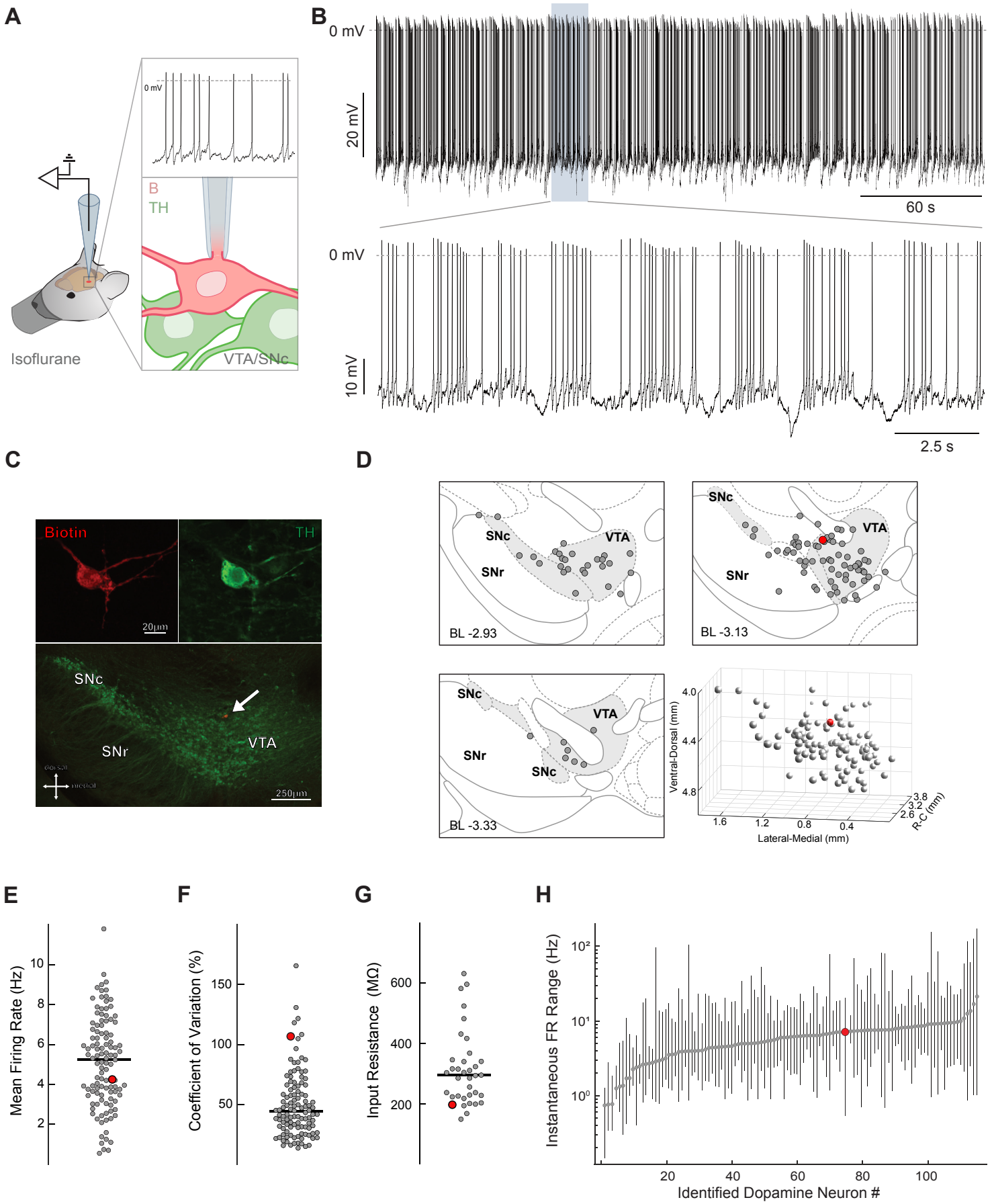
A
0 mV
B
TH
Isoflurane
VTA/SNc
B
0 mV
20 mV
60 s
0 mV
10 mV
2.5 s
C
Biotin
TH
20µm
SNc
SNr
VTA
250µm
D
SNc
VTA
SNr
BL -2.93
SNc
VTA
SNr
BL -3.13
SNc
VTA
SNr
SNc
BL -3.33
Ventral-Dorsal (mm)
4.0
4.4
4.8
1.6
1.2
0.8
0.4
Lateral-Medial (mm)
3.8
3.2
2.6
R-C (mm)
E
Mean Firing Rate (Hz)
10
8
6
4
2
F
Coefficient of Variation (%)
150
100
50
G
Input Resistance (MΩ)
600
400
200
H
Instantaneous FR Range (Hz)
10^2
10^1
10^0
20
40
60
80
100
Identified Dopamine Neuron #

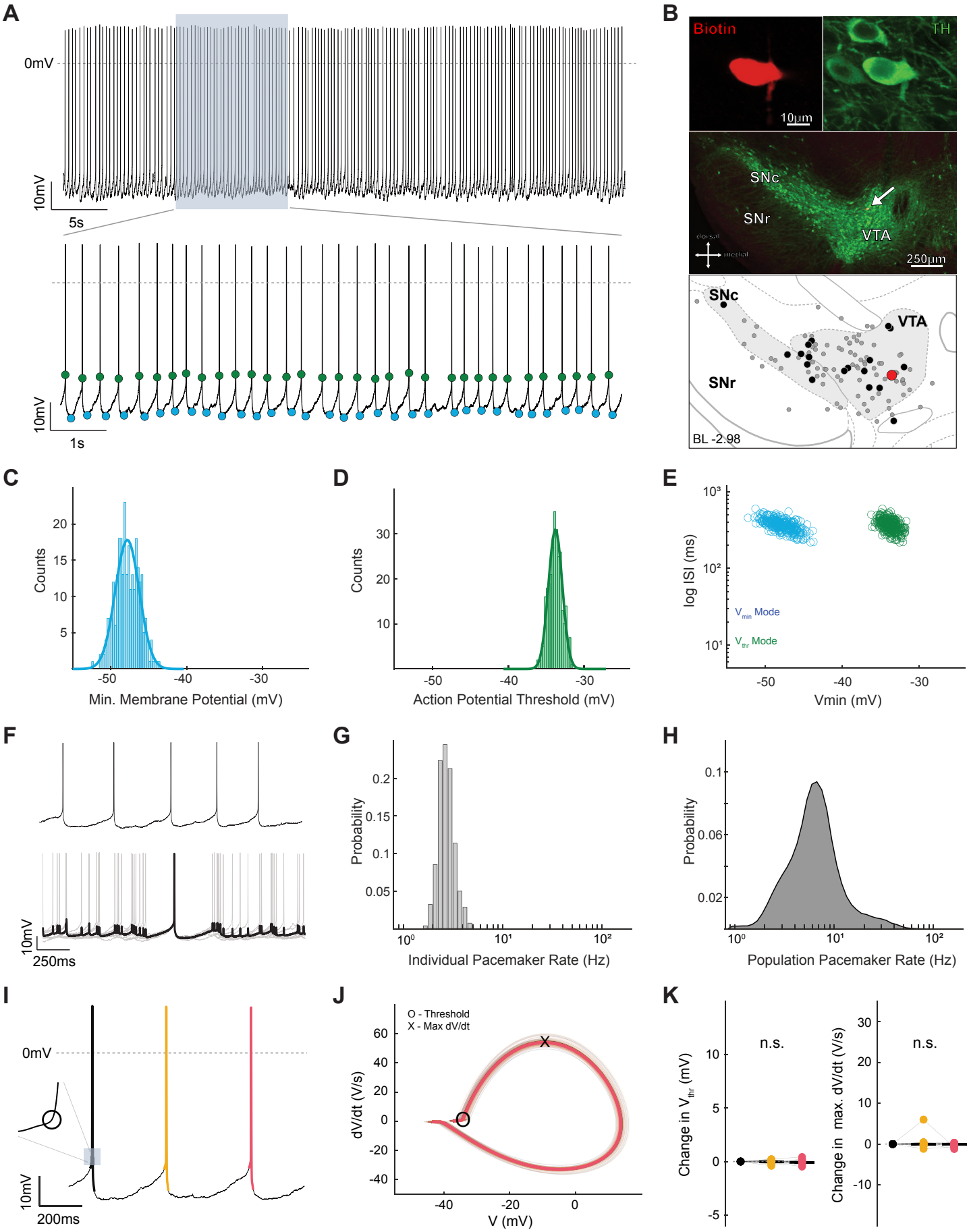
A
0mV
10mV
5s
10mV
1s
B
Biotin
TH
10µm
SNc
SNr
VTA
250µm
SNc
VTA
SNr
BL -2.98
C
Counts
Min. Membrane Potential (mV)
D
Counts
Action Potential Threshold (mV)
E
log ISI (ms)
Vmin (mV)
Vmin Mode
Vthr Mode
F
10mV
250ms
G
Probability
Individual Pacemaker Rate (Hz)
H
Probability
Population Pacemaker Rate (Hz)
I
0mV
10mV
200ms
J
O - Threshold
X - Max dV/dt
dV/dt (V/s)
V (mV)
K
Change in Vthr (mV)
n.s.
Change in max. dV/dt (V/s)
n.s.

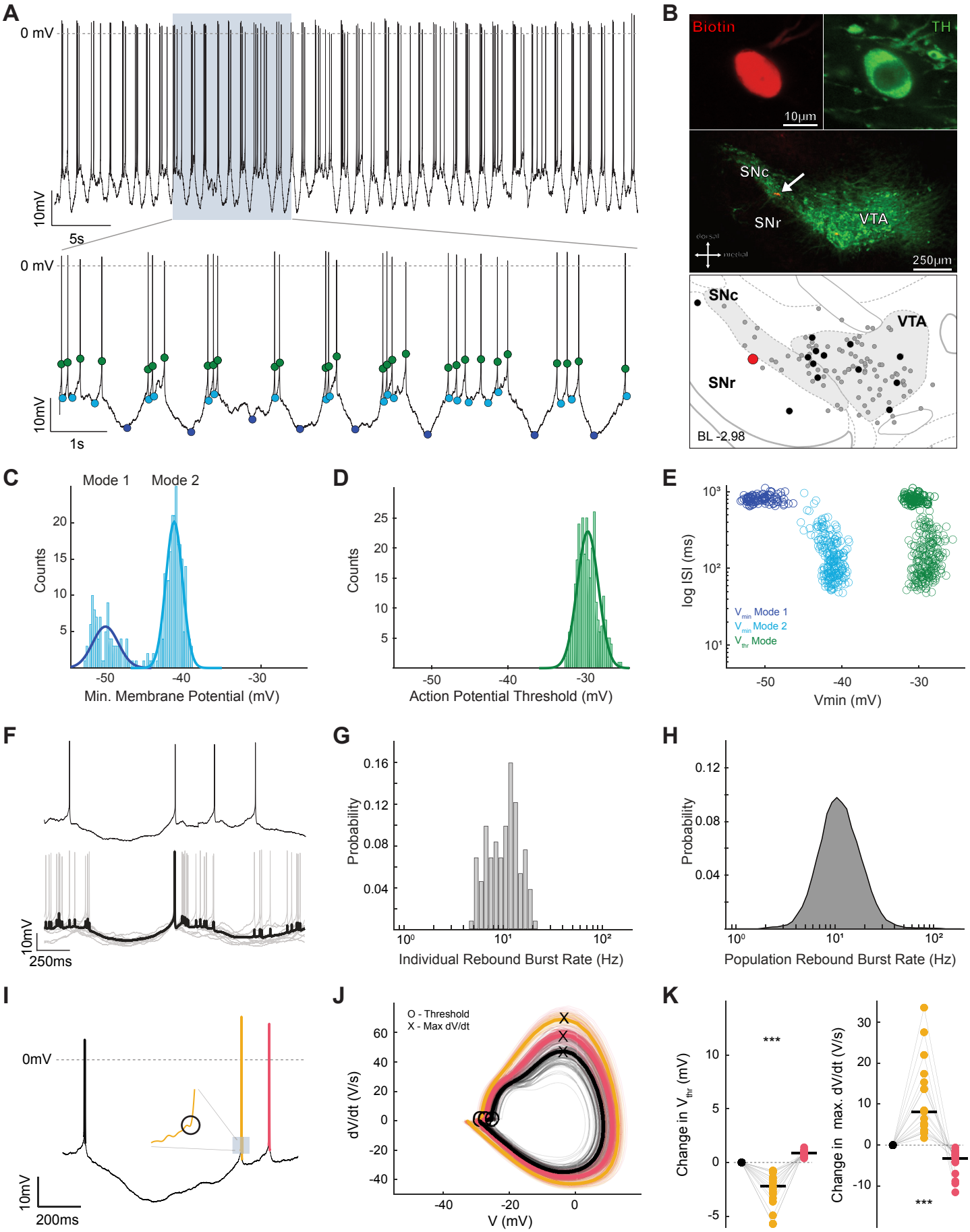
A
0 mV
10mV
5s
0 mV
10mV
1s
B
Biotin
TH
10µm
SNc
SNr
VTA
250µm
SNc
VTA
SNr
BL -2.98
C
Mode 1
Mode 2
Counts
Min. Membrane Potential (mV)
D
Counts
Action Potential Threshold (mV)
E
log ISI (ms)
Vmin (mV)
Vmin Mode 1
Vmin Mode 2
Vthr Mode
F
10mV
250ms
G
Probability
Individual Rebound Burst Rate (Hz)
H
Probability
Population Rebound Burst Rate (Hz)
I
0mV
10mV
200ms
J
O - Threshold
X - Max dV/dt
dV/dt (V/s)
V (mV)
K
Change in Vthr (mV)
***
Change in max. dV/dt (V/s)
***

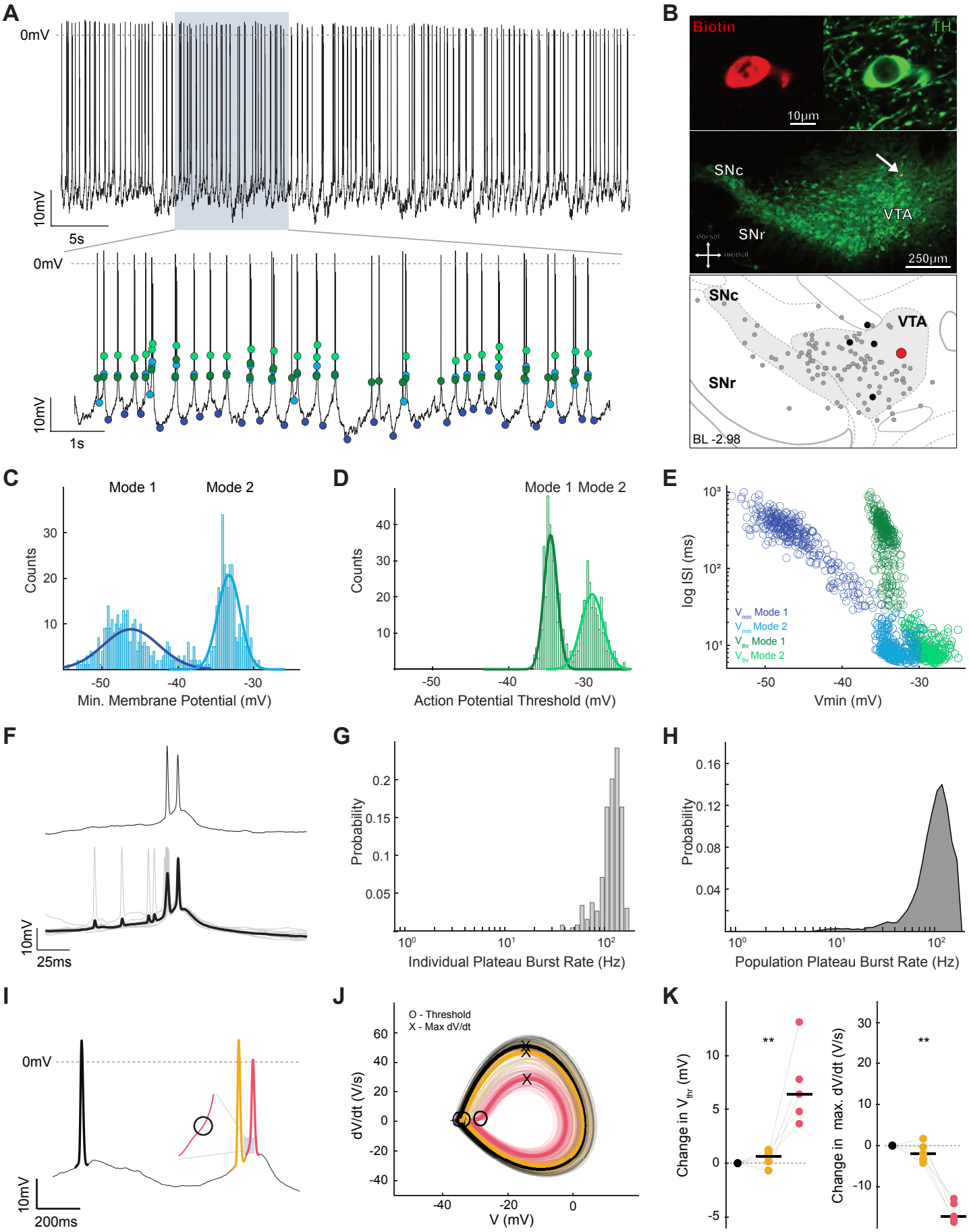
A
0mV
10mV
5s
0mV
10mV
1s
B
Biotin
TH
10µm
SNc
VTA
SNr
dorsal
medial
250µm
SNc
VTA
SNr
BL -2.98
C
Mode 1
Mode 2
Counts
Min. Membrane Potential (mV)
D
Mode 1 Mode 2
Counts
Action Potential Threshold (mV)
E
log ISI (ms)
Vmin (mV)
Vmin Mode 1
Vmin Mode 2
Vthr Mode 1
Vthr Mode 2
F
10mV
25ms
G
Probability
Individual Plateau Burst Rate (Hz)
H
Probability
Population Plateau Burst Rate (Hz)
I
0mV
10mV
200ms
J
O - Threshold
X - Max dV/dt
dV/dt (V/s)
V (mV)
K
Change in Vthr (mV)
Change in max. dV/dt (V/s)
**
**

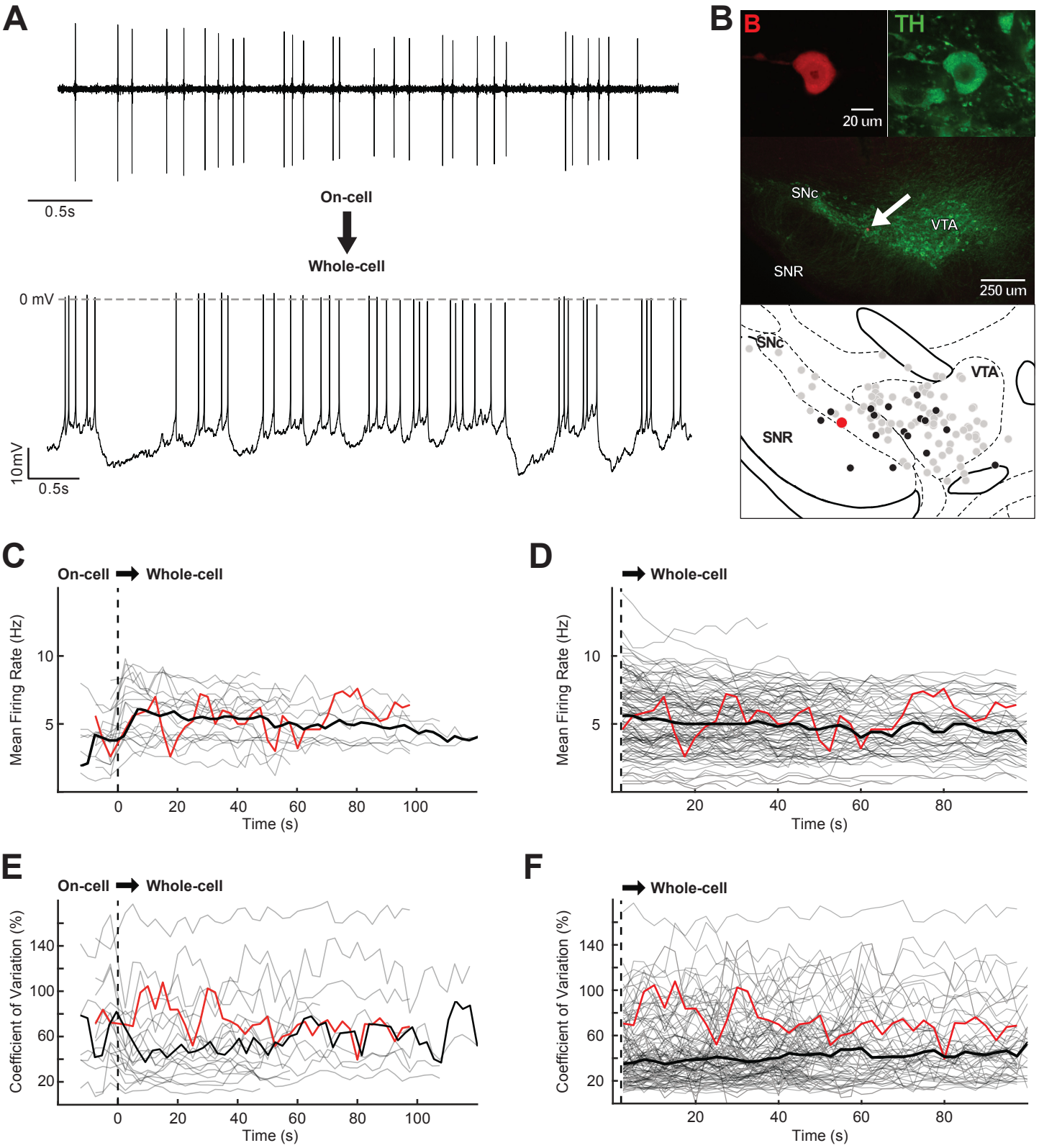
A
0.5s
On-cell
Whole-cell
0 mV
10mV
0.5s
B
B
TH
20 um
SNc
VTA
SNR
250 um
SNc
VTA
SNR
C
On-cell
Whole-cell
Mean Firing Rate (Hz)
10
5
0
20
40
60
80
100
Time (s)
D
Whole-cell
Mean Firing Rate (Hz)
10
5
20
40
60
80
Time (s)
E
On-cell
Whole-cell
Coefficient of Variation (%)
140
100
60
20
0
20
40
60
80
100
Time (s)
F
Whole-cell
Coefficient of Variation (%)
140
100
60
20
20
40
60
80
Time (s)

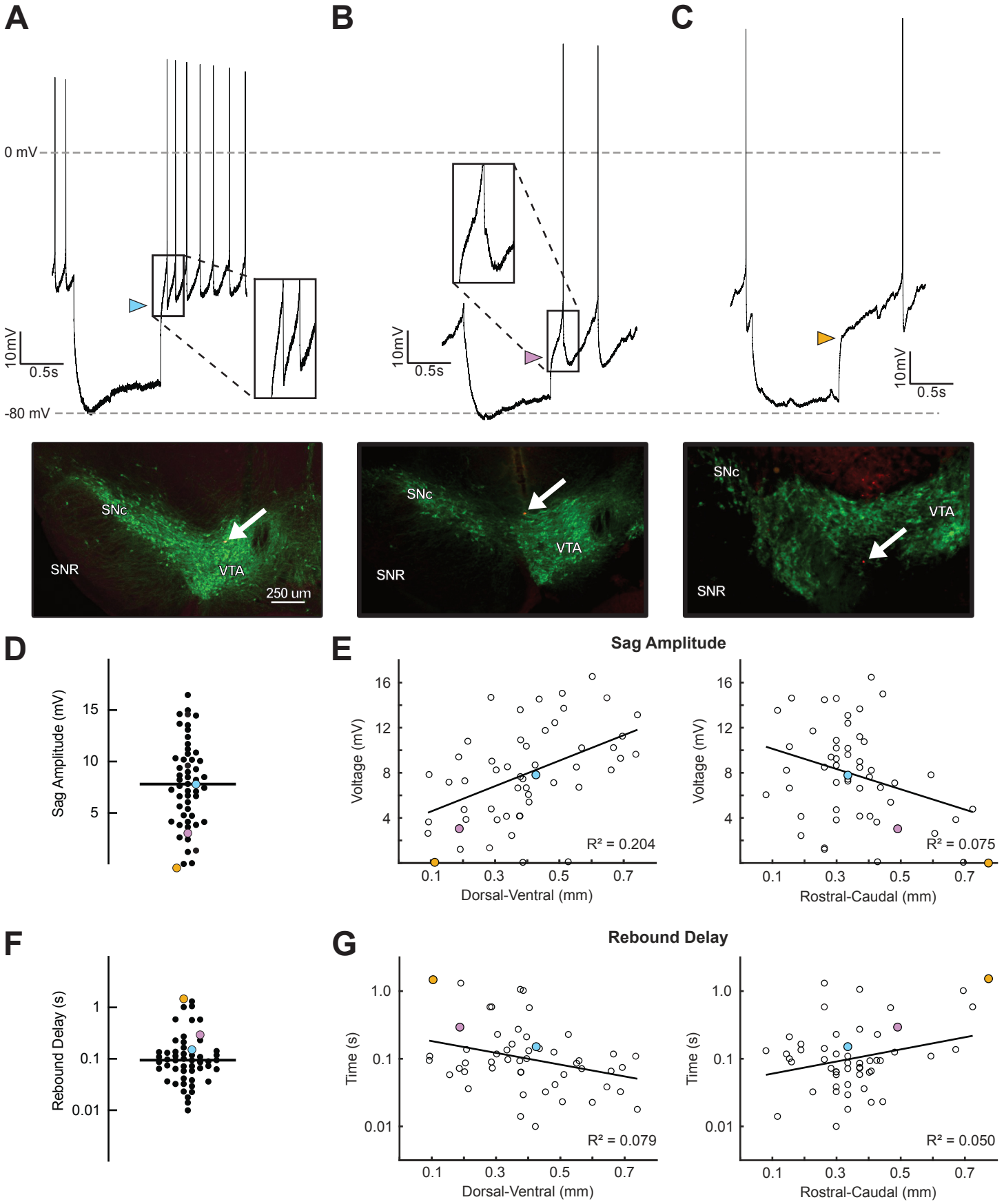
A
B
C
0 mV
-80 mV
10mV
0.5s
SNc
SNR
VTA
250 um
D
Sag Amplitude (mV)
E
Sag Amplitude
Voltage (mV)
Dorsal-Ventral (mm)
Rostral-Caudal (mm)
R² = 0.204
R² = 0.075
F
Rebound Delay (s)
G
Rebound Delay
Time (s)
R² = 0.079
R² = 0.050